International Journal of Technology



http://ijtech.eng.ui.ac.id

Research Article

Structure, Density and Hardness of Spark Plasma Sintered Fe-Mn Alloys

Sovian Aritonang^{1,**}, Andy Marjono Putranto^{1,2}, Resetiana Dwi Desiati³, Bambang Hermanto³, Michael Tulus Samuel¹, Andi Suhandi³, Oman Zuas⁴, Tony Wang⁵, Maykel T.E. Manawan^{1,3}, Toto Sudiro^{3,*}

¹Faculty of Military Mathematics and Natural Sciences, Indonesia Defense University, Bogor 16810, Indonesia;

²Organization and Human Resources Bureau, National Research and Innovation Agency, Jakarta Pusat 10340, Indonesia;

³Research Center for Advanced Material, National Research and Innovation Agency, Tangerang Selatan 15314, Indonesia;

⁴Research Center for Testing Technology and Standards, National Research and Innovation Agency, Tangerang Selatan 15314, Indonesia;

⁵Central Analytical Research Facility (CARF), Queensland University of Technology (QUT), Brisbane, QLD 4000, Australia;

*Corresponding author: toto009@brin.go.id, sovian.aritonang@idu.ac.id; Tel.: +62 81119333615; Fax.: +62 21 756 0929

Abstract: This study examines the effect of Mn content on phase evolution, density, and its correlation with the hardness of Fe-Mn alloys produced through mechanical milling followed by a spark plasma sintering technique. Alloys with Mn concentrations of 5, 10, 15, and 20 wt% were examined, revealing phase compositions primarily consisting of BCC (α -Fe, ferrite), FCC (γ -FeMn, austenite), and HCP (ε -FeMn, martensite), with minor occurrences of MnO. The Mn content significantly affected the phase distribution, strain, crystallite size, and relative density. The evolution of phase structure—particularly the balance between hard BCC, HCP, and softer FCC—emerges as a critical factor in determining hardness. The alloy with 10 wt% Mn exhibited the highest hardness (\sim 595.34 Hv) despite not having the highest density, indicating that densification and the nature and proportion of constituent phases governed the mechanical properties. While ferrite and martensite enhance hardness, increasing the Mn content promotes the formation of a more ductile austenite phase, which offsets the strengthening effects and contributes to the observed decrease in hardness at higher Mn levels. These findings highlight the complex interplay between phase transformation, microstructure, and hardness in Fe-Mn alloy systems.

Keywords: BCC; Density; Fe-Mn; Hardness; Spark plasma sintering

1. Introduction

Binary Fe-transition metal (Fe-TM) alloys, composed of iron (Fe) and elements such as chromium (Cr) (Idhil et al., 2012), cobalt (Co) (Hasegawa et al., 2017), nickel (Ni) (Xu et al., 2013), manganese (Mn) (Ekholm and Abrikosov, 2011), or molybdenum (Mo) (Chen et al., 2022) form a versatile class of materials with highly tunable properties.

Their composition and processing parameters can be precisely adjusted, enabling the development of characteristics tailored to specific needs. This adaptability has led to widespread interest in applications ranging from structural components and magnetic devices to catalytic processes.

Among these, iron–manganese (Fe–Mn)-based alloys have garnered particular attention in engineering due to their favourable physical and mechanical properties, including a pronounced shape memory effect (SME) and excellent damping capacity (Sun et al., 2019; Balagurov et al., 2018). Beyond structural uses, these alloys are also being explored for biomedical applications, especially as biodegradable implant materials (Saliba et al., 2023; Gambaro et al., 2021). Their functionality can be further optimized by varying the Mn content and incorporating alloying elements such as Cu, Si (Lemke et al., 2025), Pd (Feng et al., 2016), Ag (Krüger et al., 2022), and C (Paul et al., 2024). Incorporating manganese (Mn) in steel significantly enhances its hardenability, tensile strength, and wear resistance. However, an excessive manganese concentration, exceeding 30 wt%, can result in the formation of the brittle β -Mn phase. This phenomenon limits the suitability of the material for automotive applications (Kisku, 2024).

The Mn steels can exhibit various crystal structures, including body-centered cubic (BCC), face-centered cubic (FCC), and hexagonal close-packed (HCP) structures, allowing them to be either ferromagnetic or paramagnetic (Milititsky et al., 2008). Mn and Ni are acknowledged as austenite stabilizers in steel fabrication, playing a critical role in the expansion of the austenite phase region (Kang et al., 2021; Citrawati et al., 2020; Sabzi and Farzam, 2019; Krauss, 2015). A previous study reported that $Fe_{100-x}Mn_x$ alloys undergo distinct phase transformations contingent upon their specific compositional makeup. Specifically, alloys with compositions ranging from approximately 0 to 10 atomic percent (at%) transition from FCC to BCC structures (designated as γ - α). The phase transformation shifts from FCC to HCP configurations for compositions between 15 and 30 at% (indicated as γ - ε). The compositional range of 10–15 at% yields a complex phase structure characterized by a mixture of α and ε phases, in conjunction with the presence of both γ and ε phases (Acet et al., 1995). Medium-high manganese alloys have surged in prominence, especially through their application in twinning-induced plasticity within advanced high-strength automotive steels. In contrast, the SME, which is intrinsically linked to the reversible transformation between FCC and HCP structures in manganese steels, has further augmented interest in this research domain (Malamud et al., 2018; Milititsky et al., 2008). The evolution of the microstructure, including grain refinement and homogenization (Siripath et al., 2024), and the phase or chemical composition determine the alloy's mechanical properties (Kochmański et al., 2024; Kim et al., 2013).

Generally, FCC structures are known to have high ductility and relatively low strength compared with BCC or HCP structures. Body-centered cubic structures are typically correlated with enhanced hardness and strength; however, they may exhibit increased brittleness (Ding et al., 2024). Meanwhile, the HCP structure demonstrates significant mechanical rigidity and lack of plasticity, making it a challenging state for deformation processes. The Fe-Mn alloys can undergo phase transformations, such as FCC to HCP or BCC, which can significantly impact the alloy's overall mechanical properties, including its hardness (Wang et al., 2023). Dual-phase (DP) steels are crucial engineering materials because they offer an impressive blend of high strength and good formability. This unique combination enables the creation of lightweight and robust components suitable for various applications (Amaral et al., 2017). However, there exists a limited body of published research that systematically examines the hardness values correlated with the presence of duplex or triplex microstructural configurations within Fe-Mn alloy

systems. Consequently, comprehensively examining the influence of Mn concentration on the structural characteristics, compositional attributes, and properties of the alloy is imperative. Such an understanding is essential, as it will ultimately dictate the properties and applications of the material.

In alloy compact preparation, the integration of mechanical milling and direct current (DC) sintering, such as spark plasma sintering (SPS), represents a robust methodological approach for alloy preparation, primarily aimed at synthesizing densely packed and high-quality sintered compacts. This synergistic combination of techniques facilitates the effective manipulation of microstructural properties, thereby enhancing the resulting materials' overall performance characteristics. The SPS technique uses pulsed DC to activate and optimize sintering kinetics, offering several advantages over conventional sintering methods. Notably, SPS enables higher heating rates, reduced sintering temperatures, and diminished dwell times (Balbo and Sciti, 2008), thereby promoting a rapid sintering process conducive to the formation of fine crystalline structures and controlled grain boundary development. This technique is particularly well-suited for the consolidation of various materials, including metals, ceramics, polymers, composites (Le Godec and Le Floch, 2023), cermets, intermetallic compounds, and other advanced materials (Tokita, 2013). The SPS technique has also been employed to fabricate FeCr (Zhang et al., 2023), FeMo (Cabibbo et al., 2008), FeNi (Shongwe et al., 2016), FeCo (Mani et al., 2012), and FeMn-based alloys (Oh et al., 2018) in the context of Fe-TM alloy development, thereby underscoring its versatility and applicability within the field of materials science and engineering.

Based on the aforementioned evidence, in this study, we employed mechanical milling and SPS techniques to synthesize Fe alloys with varying Mn concentrations of 5, 10, 15, and 20 weight percent (wt%). A thorough investigation was undertaken to elucidate the effects of manganese content on the phase composition, microstructural characteristics, density, and hardness within the Fe-Mn alloy system. This research aims to contribute to a deeper understanding of how Mn concentration affects the fundamental properties of these alloys, thereby enhancing their practical applications in various industries.

2. Methods

Commercial-grade Fe and Mn powders obtained from Sigma-Aldrich (Darmstadt, Germany) with a purity of $\geq 99\%$ were used as the starting material. A series of four distinct powder compositions was prepared to evaluate the influence of varying Mn concentrations on the phase composition, microstructure, density, and hardness of the FeMn alloy. The weight percentages of Mn incorporated into the compositions were set at 5%, 10%, 15%, and 20%, respectively. These compositions were produced utilizing a mechanical milling technique, specifically employing a shaker mill PPF-UG, Ultimate Gravity (Banten, Indonesia) for 2 h with a powder-to-steel ball weight ratio of 1:4. N-hexane solution (Darmstadt, Germany) was introduced into the steel vials as a control agent to avoid agglomeration and oxidation during the milling process.

After drying, the powder mixtures were subjected to compaction through an SPS technique using Dr. Sinter SPS 625, Fuji Electronic Industrial (Japan), conducted under a vacuum environment of less than 10 Pa (Figure 1). This process was conducted with a constant applied load of 40 MPa and a heating rate of 50 °C/min. The sintering temperature was continuously monitored using a K-type thermocouple inserted within the die hole. During the sintering process, the powder displacement was systematically monitored and recorded throughout the experiment. The SPS process was deliberately halted, and the applied load was released once the sample displacement reached a sat-

uration point. Subsequently, the sample was allowed to undergo natural cooling within the chamber until it attained a temperature of less than 70 °C. The resultant sintered compact exhibited a diameter of 20 mm and a thickness of approximately 5 mm.

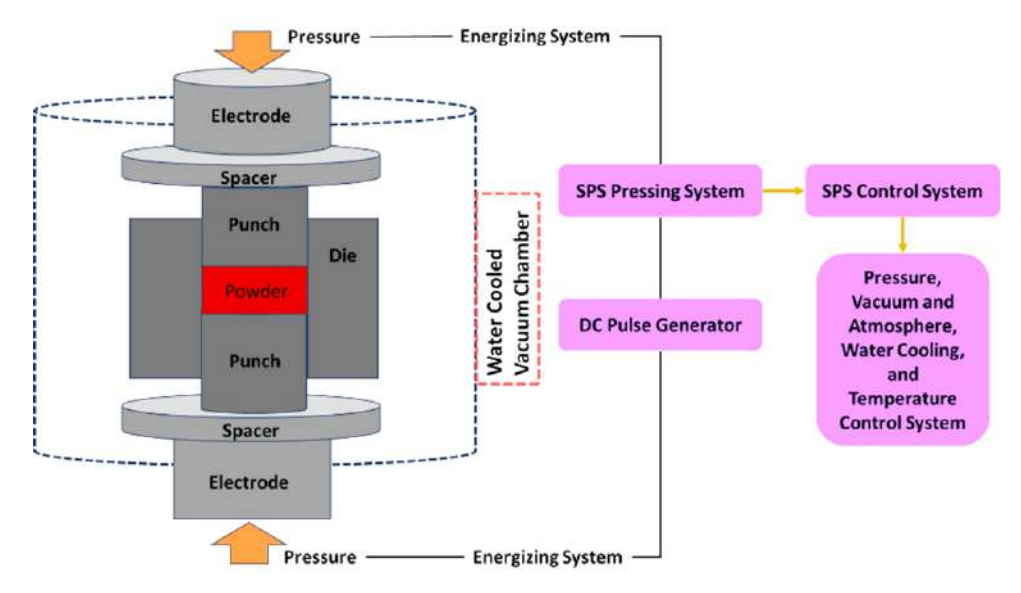


Figure 1 Schematic of the fabrication process of Fe alloys with varying Mn content using the SPS technique

To investigate and evaluate the density, phase composition, microstructure, and hardness of the sintered alloys, a systematic approach was employed. All surfaces of the samples were meticulously polished using SiC abrasive papers, followed by fine polishing with a 1 μ m alumina solution to achieve a high-quality finish. Subsequently, the polished samples underwent ultrasonic cleaning in an ethanol solution to remove any residual contaminants.

Phase composition analysis was performed using X-ray diffraction (XRD) employing Co-K α radiation on a D8 Advance diffractometer (Bruker, Germany), with a scanning rate of 0.1 s per step. The average crystallite sizes and micro-strain were initially estimated using the Williamson–Hall (W–H) method:

$$\beta cos\theta = 4\varepsilon sin\theta + \frac{\lambda}{D} \tag{1}$$

where D represents the mean crystallite size, β is the integral breadth of the diffraction peak (in radians) attributed to crystallite broadening, λ is the wavelength of the incident X-rays, θ is the Bragg angle, and ε denotes the microstrain in the lattice. The values obtained from the W–H plot served as initial estimates for subsequent Rietveld refinement. Rietveld refinement was performed using the TOPAS v7 software, incorporating a convolution-based profile fitting and the FPA (Cheary et al., 2004; Kern et al., 2004). This approach effectively subtracts instrumental broadening without the need to measure a standard sample, allowing for accurate determination of crystallite size and strain components. The mean crystallite size and micro-strain were further refined using the Double-Voigt method (Taryana et al., 2022).

The mass density of the sample was determined using Archimedes' principle, employing an analytical balance AND GF-600 (Japan) in conjunction with a density kit tester. Measurements were conducted in distilled water for 2 min to ensure consistency and accuracy. The density of a solid can be calculated based on its weight in air, the weight in

the immersion liquid, and the known density of the liquid, as follows:

$$\rho = \frac{A}{A - B} \times \rho_o \tag{2}$$

Here, ρ is the density of the sample (g/cm³), A is the weight of the sample in air (g), B is the weight of the sample in water (g), and ρ_o is the density of water at room temperature (g/cm³). Experimental comparison allowed the determination of relative density by using experimental and theoretical values. Additionally, the percentage porosity was computed as a function of the relative density, specifically through the following expression (Ayodele et al., 2021; Oladijo et al., 2019; Yan et al., 2019):

Porosity (%) =
$$(1 - \text{relative density}) \times 100\%$$
 (3)

Hardness measurements were performed using a Vickers hardness tester (Leco LM100AT, USA) with an indentation load of 300 gf and a dwell time of 13 s. To ensure statistical reliability, the reported hardness values represent the average of eight individual measurements. Microstructural characterization was performed using a scanning electron microscope (SEM)-JSM-IT200 (LA) (Japan) at an accelerating voltage of 15 kV, providing insights into the morphological features of the Fe-Mn alloy compacts. This comprehensive approach enabled a systematic investigation into how varying manganese concentrations affect the properties of the synthesized Fe-Mn alloy.

3. Results and Discussion

3.1 Spark Plasma Sintering

Figure 2 presents the sintering behaviour of Fe alloys, specifically illustrating the variation in sample thickness (stroke) as a function of time and temperature across different Mn concentration levels, prepared using the SPS technique.

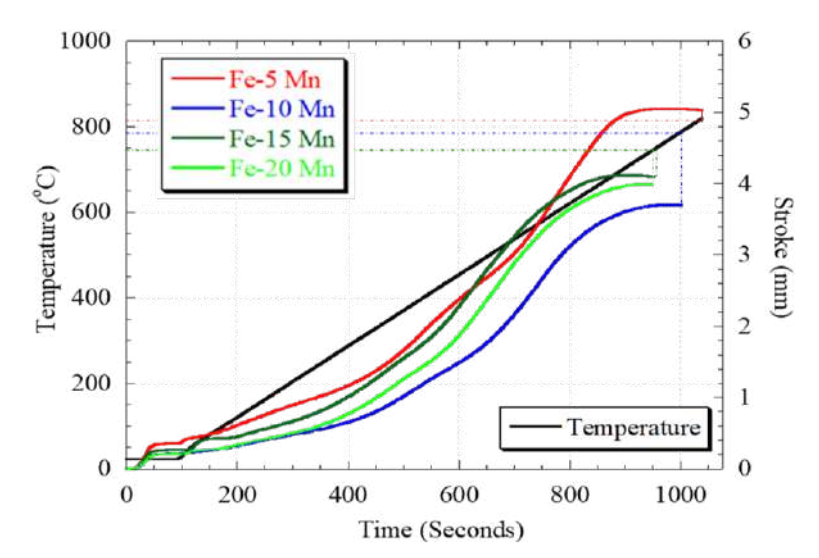


Figure 2 Sintering patterns of Fe alloys with varying Mn content prepared using the SPS technique

The displacement curves of each composition exhibit the same pattern. It tends to saturate in the temperature range of 745-820 °C, indicating that a dense structure has already been obtained. The stroke saturation change is achieved at lower temperatures with increasing Mn content. This phenomenon is attributed to the presence of Mn as

an austenite stabilizer, which effectively lowers the eutectoid temperature (Khan and Rashed, 2020; Krauss, 2015). Consequently, high-density alloys can be consolidated at lower processing temperatures.

3.2 Phase Composition

Figure 3 shows the typical XRD patterns and the constitutive phase formed on the Fe compacts with varying Mn content prepared by a SPS technique.

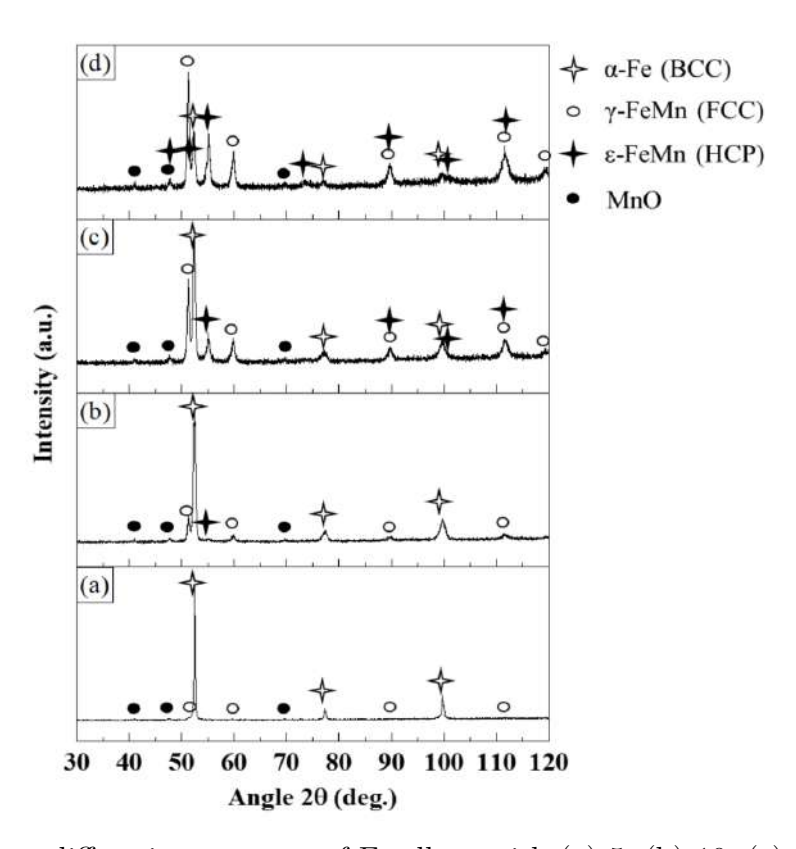


Figure 3 X-ray diffraction patterns of Fe alloys with (a) 5, (b) 10, (c) 15 and (d) 20 wt% Mn contents

The phase structure plays a critical role in determining the atomic arrangement, which subsequently governs the resulting microstructure—whether dense or porous—and thereby influences the hardness, strength, and ductility of the material. This study elucidates the effect of manganese concentration on the phase structure of Fe-Mn alloys. Specifically, these alloys exhibit a diverse range of phase configurations, including FCC, BCC, and HCP phases, which depend on the Mn content. As illustrated in the accompanying figures, an alloy composition containing 5 wt% manganese predominantly reveals a duplex microstructure characterized by both BCC and FCC phases. In contrast, an increase in Mn concentration to 10, 15, and 20 wt% leads to the development of additional HCP phases. Consequently, a more complex triplex structure—encompassing α , γ , and ε phases—emerges in alloys with elevated manganese concentrations. The distinct crystal structures and bonding characteristics of these varying phases (e.g., FCC, BCC, and HCP) impart divergent mechanical behaviors that warrant further investigation.

A notable trend in the intensity variations corresponding to each constituent phase of Fe-Mn alloys is evident in Figure 3, with a detailed semiquantitative analysis of the constituent phase presented in Figure 4.

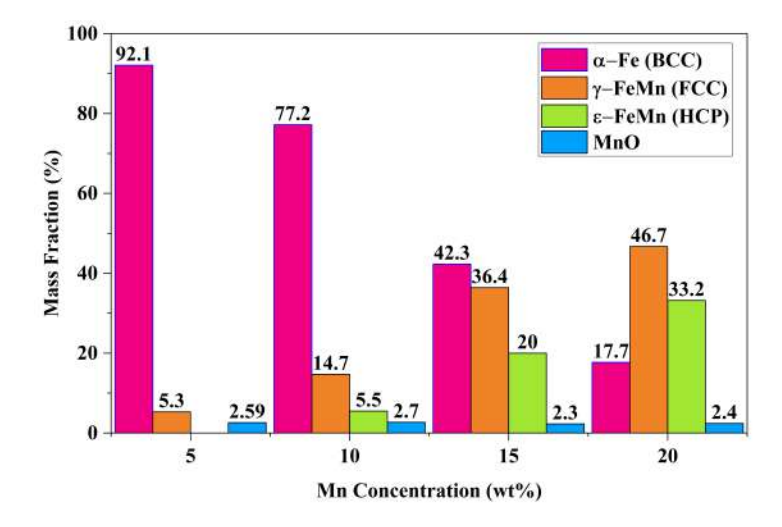


Figure 4 Mass fraction of constituent phases in Fe-Mn alloys as a function of Mn concentration

Specifically, the intensity associated with the BCC structure decreases with increasing Mn content. This observation stands in stark contrast to the intensity pattern exhibited by the FCC structure, thereby highlighting the substantial influence of Mn concentration on the stabilization and formation of austenite (Khan and Rashed, 2020; Krauss, 2015). Meanwhile, the emergence of martensite is detectable in Fe-Mn alloys with the incorporation of 10 wt% Mn, where the intensity of HCP diffraction peaks intensifies with increasing Mn concentration in the alloy. HCP or BCC formation can be linked to FCC transformation (Liu and Wu, 2024). In contrast, the broadening of the XRD peaks observed in Figure 3 may be attributed to grain refinement and the strain introduced (Oh et al., 2018) during specimen preparation. Consequently, the formation of martensite in the Fe-Mn alloys investigated in this study is predominantly influenced by the Mn content and micro-strain (Figure 5) associated with the development of a nanocrystalline structure, rather than the cooling rate. This observation holds particular significance given that the cooling process naturally transpires within a vacuum SPS chamber, mitigating the effects typically associated with rapid cooling. The observed phase transition emphasizes the critical role of Mn in altering the alloy's microstructural characteristics.

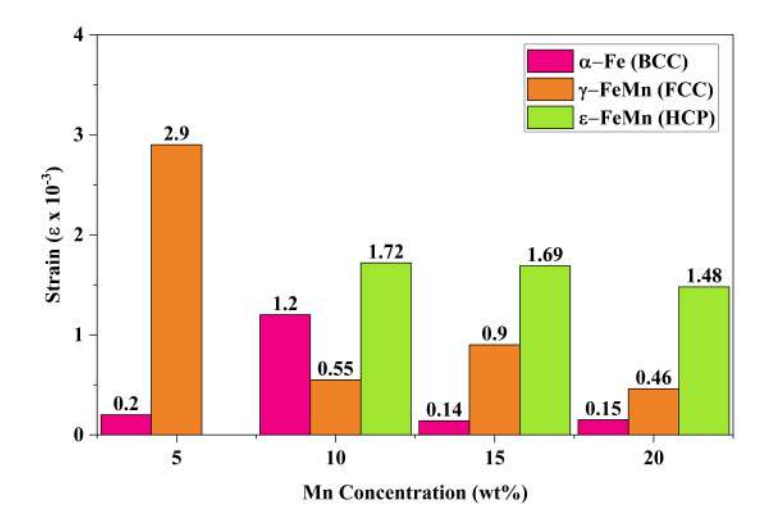


Figure 5 Strain of constituent phases in Fe-Mn alloys as a function of Mn concentration

Moreover, the XRD analysis results indicate the formation of manganese oxide (MnO) within each alloy, confirming that a minor fraction of Mn has undergone oxidation, as delineated by the relevant chemical equation below.

$$2Mn + O_2 \to 2MnO \tag{4}$$

This phenomenon is highly plausible given Mn's significant affinity for oxygen (Danninger et al., 2021). The formation of MnO further exemplifies the intricate interrelationship between alloy composition and structural transformations occurring within Fe–Mn systems. The formation of MnO inclusions with sizes of approximately 300 nm and 700 nm can enhance mechanical properties, primarily due to the Orowan strengthening mechanism (Zhang et al., 2024).

Based on the findings from the X-ray diffraction analysis, the crystallite size of each phase constituting the alloy: α (BCC), γ (FCC), and ε (HCP), was evaluated, and the results are presented in Figure 6.

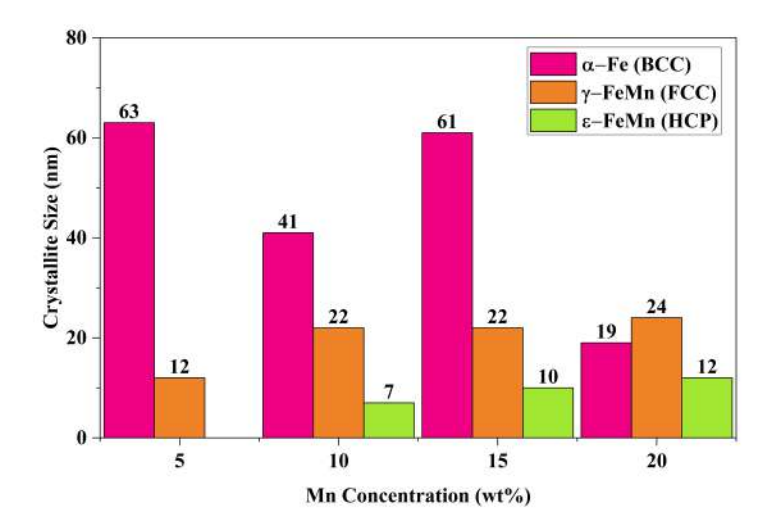


Figure 6 Crystallite size of constituent phases in Fe-Mn alloys as a function of Mn concentration

The analysis indicates that the crystalline size of the α phase exhibits a decrease with increasing Mn content. An exception arises at a composition of 10 wt% Mn, where the crystallite size of BCC is smaller than that at 15 wt% Mn. Conversely, the size of FCC crystallites generally displays an increasing trend analogous to that of HCP crystals as the Mn content increases. However, the dimensions of FCC crystals at both 10 and 15 wt% Mn are relatively comparable, and the HCP structure was not detected in the 5 wt% Mn alloy. These variations in the composition of the alloy phases, along with their respective crystallite sizes and strain, significantly influence the mechanical properties of the material, such as hardness.

3.3 Microstructure

Representative backscattered electron scanning electron microscopy (BSE SEM) images for Fe-Mn alloys exhibiting varying concentrations taken at 1000x magnification with a scale bar of 10 μ m are given in Figure 7.

As illustrated, the microstructure of the Fe-Mn alloy compacts demonstrates a predominantly dense morphology, characterized by varying Mn concentrations achieved through mechanical milling and consolidated by SPS techniques. Despite this density, the presence of pores within the alloy compact remains evident. The fraction of these pores appears to diminish with an increase in Mn content. These findings indicate that the incorporation of higher Mn concentrations contributes to the compact production of a more densely consolidated alloy.

3.4 Vickers Hardness

The correlation between the relative density and hardness of Fe-Mn alloys with Mn concentration is illustrated in Figure 8. The Archimedes density value of Fe-Mn alloys, characterized by Mn content levels of 5, 10, 15, and 20 wt%, were 7.68, 7.72, 7.78, and 7.77 g/cm³, respectively. This metric is critical for applications in which weight considerations are paramount. A comparative analysis with the theoretical density indicates a discernible trend in which the alloy's relative density increases with higher Mn concentrations. Specifically, the relative density values for the various compositions, arranged in ascending order of Mn concentration, are recorded as 97.29%, 98.04%, 99.06%, and 99.26%, respectively. These relative densities correspond to porosity levels of 2.71%, 1.96%, 0.94%, and 0.74%, respectively, calculated using Equation 3. These findings underscore a clear trend of increasing density with increasing Mn content. Moreover, the microstructural characteristics presented in Figure 7 corroborate this trend and illustrate a notable reduction in porosity with increased Mn levels.

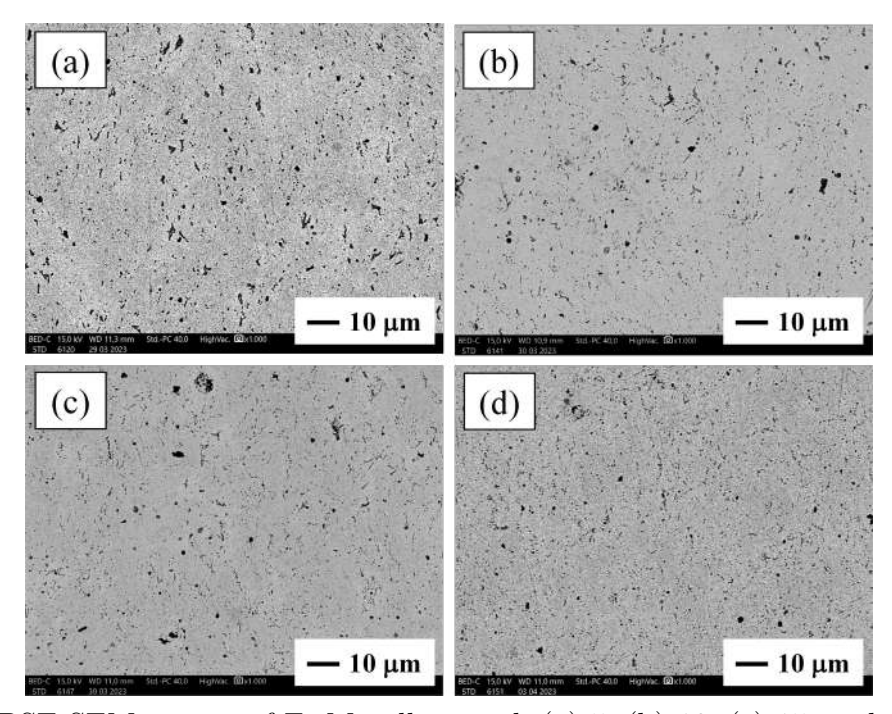


Figure 7 BSE SEM images of Fe-Mn alloys with (a) 5, (b) 10, (c) 15, and (d) 20 wt%

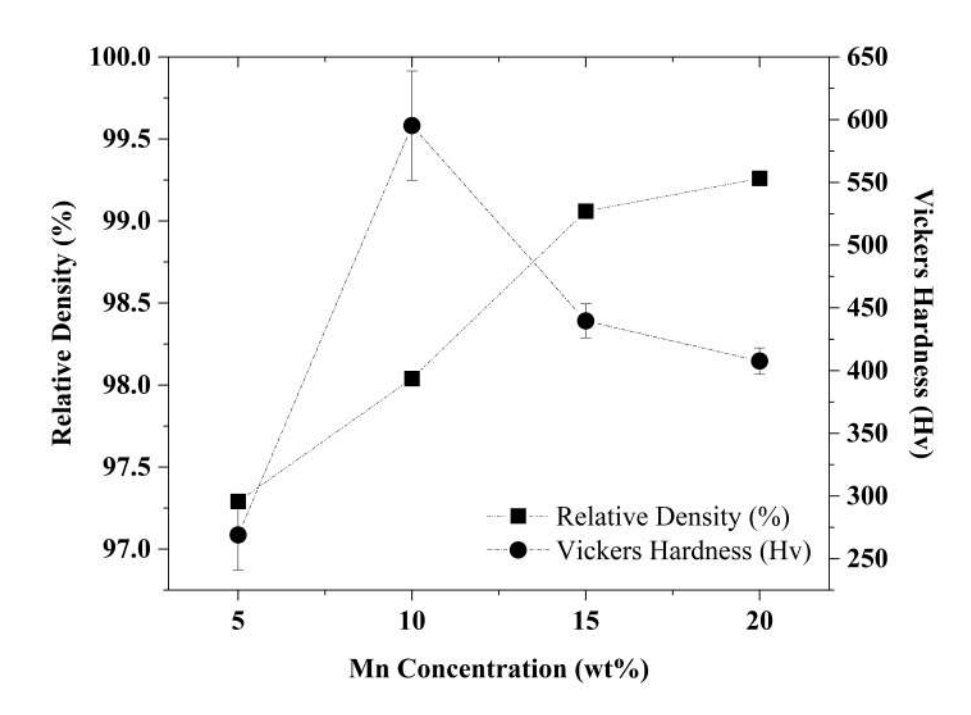


Figure 8 Relative density and Vickers hardness of Fe-Mn alloys as a function of Mn concentration

The hardness of Fe compacts with varying Mn concentrations, specifically at 5, 10, 15, and 20 wt%, was quantitatively assessed, yielding values of 268.92, 595.34, 439.60, and 407.62 Vickers hardness (Hv), respectively. Notably, the compact with 5 wt% Mn demonstrates the lowest hardness, whereas the specimen comprising 10 wt% Mn exhibits the highest hardness when compared with the other tested compositions. Hardness is a critical parameter for evaluating a material's resistance to permanent deformation, particularly in response to indentation or scratching by a harder material, and plays a vital role in quality control, material selection, and suitability determination for specific applications. The observed variation in hardness is strongly influenced by differences in phase types and their distribution within the alloy, highlighting the intricate interaction between compositional factors, microstructure, and mechanical performance in Fe-Mn systems. High-hardness alloys generally offer enhanced durability, wear resistance, and mechanical strength, making them particularly valuable in demanding engineering fields such as automotive and industrial manufacturing.

A previous study reported that the hardness of the Fe–Mn ferrite (α) phase exhibits a linear increase with Mn concentration. This phenomenon can be attributed predominantly to the lattice micro-strain, specifically the dislocations introduced during the phase transformation, which arise from the specific volume misfit between the α and γ phases (Li et al., 2002). Higher lattice strain can sometimes be associated with smaller crystallite sizes due to the increased density of crystal imperfections (Qayoom and Dar, 2020). Meanwhile, FeMnNiC alloys with varying concentrations of Mn, Ni, and C exhibited a primary microstructural composition of both γ and α phases. An increase in hardness corresponds to a reduction in the volume fraction of austenite present within these alloys (Choi et al., 2020).

In another comparison, Oh et al. (2018) investigated the hardness of Fe-x% Mn alloys (x = 4, 7, 10) produced via SPS, revealing that the hardness of the alloy containing BCC and FCC structures increased with the Mn content, specifically 25, 30, and 42 HRC

(Oh et al., 2018), or corresponding to approximately 266, 302, and 412 Hv in alignment with the hardness conversion numbers (Kuhn and Medlin, 2000). The variation in initial hardness is attributed to solid-solution strengthening from differing Mn levels and grain refinement influenced by crystallite size (Oh et al., 2018). The findings of our study indicate that the hardness of an alloy containing 5 wt% Mn is comparable to that of an alloy containing 4 wt% Mn. However, the hardness observed in the 10 wt% Mn alloy exhibits a significant deviation, which is approximately 44% higher than that in the previous study. This observation may hold particular relevance for various applications that require enhanced hardness characteristics. This could be attributed to the formation of HCP structures within the alloy, which appears to exert a substantial influence on the alloy's hardness. Superalloy austenitic steel exhibits a lower hardness than both ferritic and martensitic steel (Farihin et al., 2025). FCC exhibits a softer mechanical property than BCC iron due to its greater number of slip systems, which facilitates easier plastic deformation. In contrast, BCC iron possesses a higher hardness attributed to its more open atomic packing, resulting in fewer slip systems available for dislocation movement. This structural characteristic hinders plastic deformation, thereby enhancing hardness. Furthermore, HCP presents an intermediate number of slip systems compared to BCC and FCC structures. However, the incorporation of Mn introduces lattice distortions in Fe-Mn alloy, which increase the dislocation density and subsequently enhance the slip resistance within the material.

The findings presented in Figure 8 of this study reveal a noteworthy trend in which the hardness of the alloy decreases with increasing Mn content at 15 and 20 wt%. This trend occurred despite an observed increase in relative density. Such evidence suggests that the hardness of Fe-Mn alloys is influenced not only by relative density and porosity but also to a greater extent by the specific constitutive phases that are formed (Figure 3) and their respective phase fractions (Figure 4). While the hard HCP content increases, the softer FCC content also increases. From the results of this hardness test, the fraction of HCP in the alloy has a non-linear relationship with the measured hardness, since the softer matrix structure, namely, FCC, will significantly affect the indentation, thus leading to a decrease in the hardness of the alloy. This phenomenon is commonly observed in composite materials containing a soft matrix and hard reinforcing particles (Mola and Ren, 2018).

In addition, the strain and size of the crystallite also affect the total hardness value of the alloy. The mechanical properties, such as yield strength and hardness, strongly correlate with the grain (Abdul et al., 2021) or crystallite size of the material, as formulated by the Hall-Petch Equation (Anwar et al., 2021). They are the inverse of the square root of the grain or crystallite size. Smaller grains or crystallites exhibit greater yield strength and hardness (Yin et al., 2018; Mukhopadhyay et al., 2014). Conversely, an increase in grain size in steel is associated with a reduction in strength, while ductility tends to increase (Anwar et al., 2021). However, if the material has a relatively homogeneous microstructure, the aforementioned equation is more suitable. For the heterogeneous microstructure, deviation from the Hall-Petch prediction can be found. In addition, for the nanometer grain, a negative or inverse Hall-Petch relationship was observed, when it passed a critical grain size of about 10-30 nm (Wei et al., 2022; Naik and Walley, 2020). Therefore, the combination of phase structure, fraction, strain, and crystallite size can provide a difference in the total properties of the alloy.

In summary, the specific characteristics and functionalities of Fe-Mn alloys arise from a multifaceted relationship of factors, including manganese content, processing parameters, and structural features. These variables significantly affect key properties, such as hardness, contributing to the versatility of Fe-Mn alloys across diverse applications. Through careful control and optimization of these parameters, the mechanical and structural properties of Fe-Mn alloys can be precisely tailored to meet the requirements of various engineering and industrial uses.

4. Conclusion

Fe compacts with Mn concentrations of 5, 10, 15, and 20 wt% were successfully synthesized using mechanical milling and SPS techniques. The resulting alloy exhibits a composition characterized by BCC, FCC, and HCP structures, contingent upon the Mn content. A notable trend is observed in which the relative density of the alloy increases with increasing Mn concentrations. At 10 wt% Mn, the formation of a triplex structure—comprising BCC, FCC, and HCP phases in mass fraction ratios of 77.2%, 14.7%, and 5.5%, respectively, with 2.7% MnO—leads to the highest recorded hardness of approximately 595.34 Hv. Conversely, a decline in the alloy's hardness is noted with a reduction in the alpha phase fraction and a corresponding increase in FCC and HCP phases at 15 and 20 wt% Mn. This illustrates the complex interplay between phase composition and mechanical properties in Mn-containing Fe alloys.

Acknowledgements

This work is supported by Research Center for Advanced Material, National Research and Innovation Agency, and Fakultas Matematika dan Ilmu Pengetahuan Alam Militer (FMIPA-M), Universitas Pertahanan Indonesia. Research facilities provided by Directorate of Laboratory Management, Research Facilities, and Science and Technology Park-National Research and Innovation Agency are also gratefully acknowledged. We would also like to express our sincere gratitude to Mr. Ilham Rizki Aminudin and Mr. Mahyaruddin Mrp for their invaluable technical support.

Author Contributions

Sovian Aritonang: Conceptualization, Recourses, Data Curation, Writing-original draft, Writing review & editing. Andy Marjono Putranto: Data curation, Review. Resetiana Dwi Desiati & Bambang Hermanto: Methodology, Investigation. Michael Tulus Samuel: Data curation, Formal Analysis. Andi Suhandi & Oman Zuas: Data curation, Formal Analysis, Visualization, Writing review & editing. Tony Wang: Data curation, Formal analysis. Maykel T.E. Manawan: Data curation, Formal analysis, Validation, Visualization. Toto Sudiro: Conceptualization, Data Curation, Formal Analysis, Validation, Visualization, Writing-original draft, Writing review & editing.

Conflict of Interest

The authors declare no conflicts of interest.

References

Abdul, A., Yang, M., Shimizu, T., & Furushima, T. (2021). Effect of grain misorientation and martensitic transformation on surface roughening behavior in thin austenitic stainless steel foils. *International Journal of Technology*, 12(6), 1161–1167. https://doi.org/10.14716/ijtech.v12i6.5180

- Acet, M., Schneider, T., Gehrmann, B., & Wassermann, E. F. (1995). The magnetic aspects of the γ - α and γ - ε martensitic transformations in Fe–Mn alloys. *Journal de Physique IV*, 5, C8-379–C8-384. https://doi.org/10.1051/jp4:1995856
- Amaral, R., Santos, A. D., Sousa, J. A., & Lopes, A. B. (2017). The influence of microstructure on the mechanical behaviour of dual phase steels. In L. F. M. d. Silva (Ed.), *Materials design and applications* (pp. 25–35). Springer International Publishing. https://doi.org/10.1007/978-3-319-50784-2_3
- Anwar, M. S., Melinia, R. K., Pradisti, M. G., & Siradj, E. S. (2021). Effect of prior austenite grain-size on the annealing twin density and hardness in the austenitic stainless steel. *International Journal of Technology*, 12(6), 1149–1160. https://doi.org/10.14716/ijtech.v12i6.5190
- Ayodele, O. O., Awotunde, M. A., Babalola, B. J., & Olubambi, P. A. (2021). Spark plasma sintering of CNT–NiAl nanocomposites—process parameter, densification mechanism, and grain analysis. *Manufacturing Review*, 8, 25. https://doi.org/10.1051/mfreview/2021023
- Balagurov, A. M., Bobrikov, I. A., Pons, J., Cifre, J., Sun, L. Y., & Golovin, I. S. (2018). Structure of the Fe–Mn–Si alloys submitted to $\gamma \leftrightarrow \varepsilon$ thermocycling. *Materials Characterization*, 141, 223–228. https://doi.org/10.1016/j.matchar.2018.04.052
- Balbo, A., & Sciti, D. (2008). Spark plasma sintering and hot pressing of ZrB₂–MoSi₂ ultra-high-temperature ceramics [International Symposium on Inorganic Interfacial Engineering 2006]. *Materials Science and Engineering: A*, 475(1), 108–112. https://doi.org/https://doi.org/10.1016/j.msea.2007.01.164
- Cabibbo, M., Deodati, P., Libardi, S., Molinari, A., Montanari, R., & Ucciardello, N. (2008). Damping of FeMo alloys obtained from SPS sintering of nanostructured powders. *Materials Science Forum*, 604–605, 203–211. https://doi.org/10.4028/www.scientific.net/MSF.604-605.203
- Cheary, R. W., Coelho, A. A., & Cline, J. P. (2004). Fundamental parameters line profile fitting in laboratory diffractometers. *Journal of Research of the National Institute of Standards and Technology*, 109, 1–25. https://doi.org/10.6028/jres.109.002
- Chen, X., Duan, H., Cao, B., Sun, Q., & Yang, W. (2022). The evolution mechanism of an FeMo alloy catalyst for growth of single-walled carbon nanotubes. *Phys. Chem. Chem. Phys.*, 24, 25480–25486. https://doi.org/10.1039/D2CP03182E
- Choi, S., Jeon, J., Seo, N., Moon, Y. H., Shon, I.-J., & Lee, S.-J. (2020). Effect of composition on strain-induced martensite transformation of FeMnNiC alloys fabricated by powder metallurgy. *Archives of Metallurgy and Materials*, 65(3), 1001–1004. https://doi.org/10.24425/amm.2020.133206
- Citrawati, F., Dwiwandono, R., & Firmansyah, L. (2020). The effect of Ni on the formation of bainite in Fe–Ni lateritic steels through semi-continuous cooling method. International Journal of Technology, 11(1), 60–70. https://doi.org/10.14716/ijtech.v11i1.3178
- Danninger, H., Gierl-Mayer, C., Prokofyev, M., Huemer, M.-C., De Oro Calderon, R., Hellein, R., Müller, A., & Stetina, G. (2021). Manganese—a promising element also in high alloy sintered steels. *Powder Metallurgy*, 64(2), 115–125. https://doi.org/10.1080/00325899.2021.1886717
- Ding, Z., Ding, C., Yang, Z., Zhang, H., Wang, F., Li, H., Xu, J., Shan, D., & Guo, B. (2024). Ultra-high strength in FCC+BCC high-entropy alloy via different gradual morphology. *Materials*, 17(18). https://doi.org/10.3390/ma17184535

- Ekholm, M., & Abrikosov, I. A. (2011). Structural and magnetic ground-state properties of γ -femn alloys from ab initio calculations. *Phys. Rev. B*, 84, 104423. https://doi.org/10.1103/PhysRevB.84.104423
- Farihin, P., Suharno, B., Dani, M., Ngarayana, I. W., Andryansyah, Insani, A., Wardana, R. I., Huang, C. A., Aziz, F., & Adhika, D. R. (2025). High-resolution neutron diffraction analysis of residual stresses in oxide dispersion strengthened FeNiCrY₂O₃ cast alloys for advanced nuclear reactor applications. *International Journal of Technology*, 16(2), 625–638. https://doi.org/10.14716/ijtech.v16i2.7241
- Feng, Y. P., Blanquer, A., Fornell, J., Zhang, H., Solsona, P., Baró, M. D., Suriñach, S., Ibáñez, E., García-Lecina, E., Wei, X., Li, R., Barrios, L., Pellicer, E., Nogués, C., & Sort, J. (2016). Novel Fe–Mn–Si–Pd alloys: Insights into mechanical, magnetic, corrosion resistance and biocompatibility performances. J. Mater. Chem. B, 4, 6402–6412. https://doi.org/10.1039/C6TB01951J
- Gambaro, S., Paternoster, C., Occhionero, B., Fiocchi, J., Biffi, C., Tuissi, A., & Mantovani, D. (2021). Mechanical and degradation behavior of three Fe-Mn-C alloys for potential biomedical applications. *Materials Today Communications*, 27, 102250. https://doi.org/https://doi.org/10.1016/j.mtcomm.2021.102250
- Hasegawa, T., Kanatani, S., Kazaana, M., Takahashi, K., Kumagai, K., Hirao, M., & Ishio, S. (2017). Conversion of FeCo from soft to hard magnetic material by lattice engineering and nanopatterning. *Scientific Reports*, 7, 13215. https://doi.org/10.1038/s41598-017-13602-x
- Idhil, A., Borca, C., Uldry, A.-C., Zema, N., Turchini, S., Catone, D., Foelske, A., Grolimund, D., & Samaras, M. (2012). The influence of Cr composition on the local magnetic structure of FeCr alloys. *Nuclear Instruments and Methods in Physics Research Section B: Beam Interactions with Materials and Atoms*, 284, 1–5. https://doi.org/https://doi.org/10.1016/j.nimb.2011.08.071
- Kang, L., Yuan, H., Li, H., Ji, Y., Liu, H., & Liu, G. (2021). Enhanced mechanical properties of Fe-Mn-Al-C low density steel via aging treatment. Frontiers in Materials, 8. https://doi.org/10.3389/fmats.2021.680776
- Kern, A., Coelho, A. A., & Cheary, R. W. (2004). Convolution based profile fitting. In E. J. Mittemeijer & P. Scardi (Eds.), Diffraction analysis of the microstructure of materials (pp. 17–50). Springer Berlin Heidelberg. https://doi.org/10.1007/978-3-662-06723-9_2
- Khan, F., & Rashed, H. M. M. A. (2020). Phase transformation in micro-alloyed steels. In A. Sharma, Z. Duriagina, & S. Kumar (Eds.), *Engineering steels and high entropy alloys*. IntechOpen. https://doi.org/10.5772/intechopen.91468
- Kim, H., Suh, D.-W., & Kim, N. J. (2013). Fe–al–mn–c lightweight structural alloys: A review on the microstructures and mechanical properties. *Science and Technology of Advanced Materials*, 14, 014205. https://doi.org/10.1088/1468-6996/14/1/014205
- Kisku, N. (2024). Development of novel low density ultra-high strength manganese-steel with significant ductility through thermo-mechanical processing route. *Materials Science and Engineering: A*, 901, 146591. https://doi.org/https://doi.org/10.1016/j.msea.2024.146591
- Kochmański, P., Chylińska, R., Figiel, P., Fryska, S., Kochmańska, A. E., Kwiatkowska, M., Kwiatkowski, K., Niemczyk, A., Słowik, J., Maziarz, W., Rogal, Ł., Dybowski, K., & Baranowska, J. (2024). Influence of chemical composition on structure and mechanical properties of vacuum-carburized low-alloy steels. *Materials*, 17(2). https://doi.org/10.3390/ma17020515

- Krauss, G. (2015). Steels: Processing, structure, and performance (2nd ed.). ASM International. https://doi.org/10.31399/asm.tb.spsp2.9781627082655
- Krüger, J. T., Hoyer, K.-P., Huang, J., Filor, V., Mateus-Vargas, R. H., Oltmanns, H., Meißner, J., Grundmeier, G., & Schaper, M. (2022). FeMn with phases of a degradable Ag alloy for residue-free and adapted bioresorbability. *Journal of Functional Biomaterials*, 13(4). https://doi.org/10.3390/jfb13040185
- Kuhn, H., & Medlin, D. (2000). Mechanical testing and evaluation (Vol. 8). ASM International. https://doi.org/10.31399/asm.hb.v08.9781627081764
- Le Godec, Y., & Le Floch, S. (2023). Recent developments of high-pressure spark plasma sintering: An overview of current applications, challenges and future directions. *Materials*, 16(3). https://www.mdpi.com/1996-1944/16/3/997
- Lemke, J. N., Fiocchi, J., Biffi, C. A., Tuissi, A., Copes, F., Paternoster, C., Mantovani, D., & Coda, A. (2025). Design, development and performance of a Fe–Mn–Si–Cu alloy for bioabsorbable medical implants. *Journal of Materials Chemistry B*, 13, 2737–2752. https://doi.org/10.1039/D4TB01635A
- Li, C.-M., Sommer, F., & Mittemeijer, E. J. (2002). Characteristics of the $\gamma \to \alpha$ transformation in Fe-Mn alloys. Materials Science and Engineering: A, 325(1), 307–319. https://doi.org/https://doi.org/10.1016/S0921-5093(01)01459-9
- Liu, T.-W., & Wu, X.-L. (2024). Martensitic transformation pathways and crystallographic orientation relationships in steel. *Journal of Materials Science & Technology*, 174, 74–84. https://doi.org/https://doi.org/10.1016/j.jmst.2023.06.060
- Malamud, F., Guerrero, L., La Roca, P., Sade, M., & Baruj, A. (2018). Role of Mn and Cr on structural parameters and strain energy during FCC-HCP martensitic transformation in Fe-Mn-Cr shape memory alloys. *Materials & Design*, 139, 314–323. https://doi.org/https://doi.org/10.1016/j.matdes.2017.11.017
- Mani, M. K., Viola, G., Reece, M. J., Hall, J. P., & Evans, S. L. (2012). Structural and magnetic characterization of spark plasma sintered Fe–50Co alloys. *MRS Online Proceedings Library*, 1516, 201–207. https://doi.org/10.1557/opl.2012.1669
- Milititsky, M., Van Caenegem, N., & De Cooman, B. C. (2008). Structural and magnetic transformations in the Fe–Mn binary system. *Steel Research International*, 79, 156–159. https://doi.org/10.1002/srin.200806331
- Mola, J., & Ren, M. (2018). On the hardness of high carbon ferrous martensite. *IOP Conference Series: Materials Science and Engineering*, 373, 012004. https://doi.org/10.1088/1757-899X/373/1/012004
- Mukhopadhyay, N. K., Ali, F., Scudino, S., Samadi Khoshkhoo, M., Stoica, M., Srivastava, V. C., Uhlenwinkel, V., Vaughan, G., Suryanarayana, C., & Eckert, J. (2014). Inverse hall–petch-like mechanical behaviour in nanophase Al–Cu–Fe quasicrystals: A new phenomenon. *Acta Physica Polonica A*, 126, 543–548. https://doi.org/10.12693/APhysPolA.126.543
- Naik, S. N., & Walley, S. M. (2020). The hall–petch and inverse hall–petch relations and the hardness of nanocrystalline metals. *Journal of Materials Science*, 55, 2661–2681. https://doi.org/10.1007/s10853-019-04160-w
- Oh, S.-J., Park, D., Kim, K., Shon, I.-J., & Lee, S.-J. (2018). Austenite stability and mechanical properties of nanocrystalline Fe–Mn alloy fabricated by spark plasma sintering with variable Mn content. *Materials Science and Engineering: A*, 725, 382–388. https://doi.org/https://doi.org/10.1016/j.msea.2018.04.051
- Oladijo, O., Popoola, A., Ujah, C., & Namoshe, M. (2019). Dataset of spark plasma sintering of Al-Zn-Sn alloy for soft solder application. *Data in Brief*, 24, 103948. https://doi.org/https://doi.org/10.1016/j.dib.2019.103948

- Paul, B., Kiel, A., Otto, M., Gemming, T., Hoffmann, V., Giebeler, L., Kaltschmidt, B., Hütten, A., Gebert, A., Kaltschmidt, C., & Hufenbach, J. (2024). Inherent antibacterial properties of biodegradable FeMnC(Cu) alloys for implant application. *ACS Applied Bio Materials*, 7, 839–852. https://doi.org/10.1021/acsabm.3c00835
- Qayoom, M., & Dar, G. N. (2020). Crystallite size and compressive lattice strain in NiFe₂O₄ nanoparticles as calculated in terms of various models: Influence of annealing temperature. *International Journal of Self-Propagating High-Temperature Synthesis*, 29, 213–219. https://doi.org/10.3103/S1061386220040111
- Sabzi, M., & Farzam, M. (2019). Hadfield manganese austenitic steel: A review of manufacturing processes and properties. *Materials Research Express*, 6, 1065c2. https://doi.org/10.1088/2053-1591/ab3ee3
- Saliba, L., Sammut, K., Tonna, C., Pavli, F., Valdramidis, V., Gatt, R., Giordmaina, R., Camilleri, L., Atanasio, W., Buhagiar, J., & Schembri Wismayer, P. (2023). FeMn and FeMnAg biodegradable alloys: An in vitro and in vivo investigation. *Heliyon*, 9(5), e15671. https://doi.org/https://doi.org/10.1016/j.heliyon.2023.e15671
- Shongwe, M., Ramakokovhu, M., Diouf, S., Durowoju, M., Obadele, B., Sule, R., Lethabane, M., & Olubambi, P. (2016). Effect of starting powder particle size and heating rate on spark plasma sintering of FeNi alloys. *Journal of Alloys and Compounds*, 678, 241–248. https://doi.org/https://doi.org/10.1016/j.jallcom.2016.03.270
- Siripath, N., Suranuntchai, S., & Sucharitpwatskul, S. (2024). Modeling dynamic recrystallization kinetics in BS 080M46 medium carbon steel: Experimental verification and finite element simulation. *International Journal of Technology*, 15(5), 1292–1307. https://doi.org/10.14716/ijtech.v15i5.6770
- Sun, L., Cheverikin, V., & Golovin, I. (2019). Mechanical spectroscopy as an in situ tool to study anelasticity of martensitic transition in Fe-16Mn-8Cr-2Co alloy. *Materials Letters*, 256, 126635. https://doi.org/https://doi.org/10.1016/j.matlet.2019. 126635
- Taryana, Y., Wahyu, Y., Manaf, A., Manawan, M., & Ariadi, W. (2022). Structural and microwave absorption properties of $BaFe_{12-2x}Sn_xZn_xO_{19}$ (x=0.05-1.0) ceramic magnets. Materialia, 23, 101455. https://doi.org/10.1016/j.mtla.2022.101455
- Tokita, M. (2013). Spark plasma sintering (SPS) method, systems, and applications. In $Handbook\ of\ advanced\ ceramics$ (pp. 1149–1177). Elsevier. https://doi.org/10.1016/B978-0-12-385469-8.00060-5
- Wang, Y., Wu, C., Liu, Y., Tian, M., Lu, X., & Su, X. (2023). Insight into the FCC→HCP transformation in Co-rich Co-Cr-Fe-Mn-Ni high-entropy alloys. *Metals*, 13(3). https://doi.org/10.3390/met13030504
- Wei, F., Cheng, B., Chew, L. T., Lee, J. J., Cheong, K. H., Wu, J., Zhu, Q., & Tan, C. C. (2022). Grain distribution characteristics and effect of diverse size distribution on the hall–petch relationship for additively manufactured metal alloys. *Journal of Materials Research and Technology*, 20, 4130–4136. https://doi.org/https://doi.org/10.1016/j.jmrt.2022.09.006
- Xu, Z., Jin, C., Xia, A., Zhang, J., & Zhu, G. (2013). Structural and magnetic properties of nanocrystalline nickel-rich Fe–Ni alloy powders prepared via hydrazine reduction. Journal of Magnetism and Magnetic Materials, 336, 14–19. https://doi.org/https://doi.org/10.1016/j.jmmm.2013.02.007
- Yan, X., Li, Q., Yin, S., Chen, Z., Jenkins, R., Chen, C., Wang, J., Ma, W., Bolot, R., Lupoi, R., Ren, Z., Liao, H., & Liu, M. (2019). Mechanical and in vitro study of an isotropic Ti6Al4V lattice structure fabricated using selective laser melting.

- Journal of Alloys and Compounds, 782, 209–223. https://doi.org/https://doi.org/10.1016/j.jallcom.2018.12.220
- Yin, F., Cheng, G. J., Xu, R., Zhao, K., Li, Q., Jian, J., Hu, S., Sun, S., An, L., & Han, Q. (2018). Ultrastrong nanocrystalline stainless steel and its hall-petch relationship in the nanoscale. *Scripta Materialia*, 155, 26–31. https://doi.org/https://doi.org/10.1016/j.scriptamat.2018.06.014
- Zhang, X., Zhao, Q., Liu, C., Peng, Y., Huang, Y., Kong, J., & Wang, K. (2024). On the formation of oxide inclusions in the high nitrogen chromium-manganese steel produced by the wire and arc additive manufacturing. *Journal of Materials Research and Technology*, 33, 3852–3863. https://doi.org/https://doi.org/10.1016/j.jmrt. 2024.10.103
- Zhang, X., Wang, Q., Kane, J. J., Rufner, J. F., & Sun, C. (2023). Graded microstructure and mechanical properties of spark plasma sintered Fe-Cr alloys. *Journal of Alloys and Compounds*, 967, 171448. https://doi.org/https://doi.org/10.1016/j.jallcom. 2023.171448